

Ion and Electron Acceleration in Fully Kinetic Plasma Turbulence

LUCA COMISSO¹ AND LORENZO SIRONI¹

¹*Department of Astronomy and Columbia Astrophysics Laboratory, Columbia University, New York, NY 10027, USA*

ABSTRACT

Turbulence is often invoked to explain the origin of nonthermal particles in space and astrophysical plasmas. By means of 3D fully kinetic particle-in-cell simulations, we demonstrate that turbulence in low- β plasmas (β is the ratio of plasma pressure to magnetic pressure) accelerates ions and electrons into a nonthermal energy distribution with a power-law energy range. The ion spectrum is harder than the electron one, and both distributions get steeper for higher β . We show that the energization of electrons is accompanied by a significant energy-dependent pitch-angle anisotropy, with most electrons moving parallel to the local magnetic field, while ions stay roughly isotropic. We demonstrate that particle injection from the thermal pool occurs in regions of high current density. Parallel electric fields associated with magnetic reconnection are responsible for the initial energy gain of electrons, whereas perpendicular electric fields control the overall energization of ions. Our findings have important implications for the origin of nonthermal particles in space and astrophysical plasmas.

1. INTRODUCTION

Nonthermal energetic particles are ubiquitous in space and astrophysical environments. The solar corona and wind (McComas et al. 2019), supernova remnants (Reynolds 2008), accretion disk coronae (Yuan & Narayan 2014), jets from supermassive black holes (Blandford et al. 2019), and galaxy clusters (Brunetti & Jones 2014) are just a few examples where the presence of energetic particles, often in the form of power-law distributions, is observed or inferred. However, their origin is still poorly understood. Among the potential processes responsible for their acceleration, turbulence in collisionless plasmas is often invoked as a prime candidate (Melrose 1980; Lazarian et al. 2012; Petrosian 2012).

The idea that magnetized turbulence could lead to a power-law energy distribution of accelerated particles can be traced back to Fermi's original model of stochastic particle acceleration through repeated interactions with moving magnetized structures (Fermi 1949). Following Fermi's insight, the development of quasilinear theory (e.g. Kennel & Engelmann 1966; Hall & Sturrock 1967; Kulsrud & Ferrari 1971; Achterberg 1981; Jaekel & Schlickeiser 1992) and its nonlinear extensions (e.g.

Völk 1973; Bieber & Matthaeus 1997; Matthaeus et al. 2003; Shalchi 2006; Yan & Lazarian 2008) have deepened our understanding of particle acceleration in turbulence. On the other hand, these simplified analytical models neglect some important aspects of the physics of turbulence. Above all, they ignore the role of magnetic reconnection, which is an essential component of particle acceleration in a magnetized turbulent cascade (Arzner & Vlahos 2004; Dmitruk et al. 2004; Kowal et al. 2012; Comisso & Sironi 2018, 2019).

In order to address this problem in all its complexity, fully kinetic numerical simulations are necessary. This has recently been possible in the relativistic regime (Zhankin et al. 2017; Comisso & Sironi 2018, 2019; Zhankin et al. 2018, 2019; Comisso et al. 2020; Wong et al. 2020; Comisso & Sironi 2021; Näätälä & Beloborodov 2021; Sobacchi et al. 2021), where the Alfvén speed approaches the speed of light and computational costs are substantially reduced. In the non-relativistic regime, progress has been made through test-particle simulations in synthetic turbulence (e.g. Michałek & Ostrowsky 1996; Arzner et al. 2006; O'Sullivan et al. 2009; Teraki & Asano 2019) or fluid-type simulations (e.g. Arzner & Vlahos 2004; Dmitruk et al. 2004; Lehe et al. 2009; Kowal et al. 2012; Dalena et al. 2014; Lynn et al. 2014; Beresnyak & Li 2016; González et al. 2017; Isliker et al. 2017; Kimura et al. 2019; Trotta et al. 2020; Sun & Bai 2021; Pezzi et al. 2022), and, more recently, through hybrid fluid-kinetic simulations (e.g. Kunz et al.

2016; Pecora et al. 2018; Arzamasskiy et al. 2019). However, these approaches suffer from important limitations: test-particle calculations neglect the back-reaction of accelerated particles onto the electromagnetic fields, and they need to employ ad hoc prescriptions for particle injection; the hybrid fluid-kinetic approach describes electrons merely as a fluid. The kinetic physics of both ions and electrons is needed to properly account for magnetic reconnection in a collisionless plasma and to self-consistently capture the energization of both species.

In this Letter, we investigate the self-consistent acceleration of ions and electrons in a turbulent plasma. We consider a low- β plasma, which is relevant for various space and astrophysical systems, such as the solar corona or accretion disk coronae. We demonstrate that turbulence naturally produces nonthermal tails with a power-law energy range for both ions and electrons. We show that particles are extracted from the thermal pool in regions of high current density associated with magnetic reconnection, and that the different acceleration mechanisms responsible for the energization of ions and electrons leave a distinctive signature on their pitch-angle distributions.

2. NUMERICAL METHOD AND SETUP

We adopt a first-principles approach by solving the coupled Vlasov-Maxwell system of equations through the particle-in-cell (PIC) method (Birdsall & Langdon 1985) with TRISTAN-MP (Buneman 1993; Spitkovsky 2005). We perform the numerical simulations in a triply periodic cubic domain L^3 that is discretized into a regular lattice of 1400^3 cells. The initial conditions correspond to uniform plasma with total particle density $2n_0$, Maxwellian-distributed ions and electrons of equal temperature $T_{i0} = T_{e0} = T_0$, and uniform guide magnetic field $\mathbf{B}_0 = B_0 \hat{\mathbf{z}}$. Turbulence is seeded by initializing a spectrum of magnetic fluctuations having polarizations transverse to \mathbf{B}_0 (see Comisso & Sironi (2018, 2019) for details). The root-mean-square amplitude of the fluctuations is $\delta B_0 = B_0$, where $\delta B_0 = \langle \delta B^2(t=0) \rangle^{1/2}$. The energy-carrying scale is $l = L/3$.

We resolve the electron skin depth $d_e = c/\omega_{pe}$ with 3.3 cells and employ an average of 64 computational particles per cell. In order to capture the full turbulent cascade from MHD scales to electron kinetic scales, we use a reduced ion-to-electron mass ratio of $m_i/m_e = 50$, which gives a domain size $L/d_i = 60$, where $d_i = c/\omega_{pi}$ is the ion inertial length, with $\omega_{pi} = (4\pi n_0 e^2/m_i)^{1/2}$ indicating the ion plasma frequency. The ratio of electron plasma frequency $\omega_{pe} = (4\pi n_0 e^2/m_e)^{1/2}$ to electron gyrofrequency $\omega_{ce} = eB_0/m_e c$ is $\omega_{pe}/\omega_{ce} = 1$, as expected in the solar corona. Then, the Alfvén speed

is $v_A = B_0/(4\pi n_0 m_i)^{1/2} = 0.14c$. We consider a low- β plasma, with β_0 ranging from 0.32 down to 0.04. Here, $\beta_0 = \beta_{i0} + \beta_{e0}$ is the initial total plasma β , with $\beta_{i0} = \beta_{e0} = 8\pi n_0 k_B T_0/B_0^2$. We scan β_0 by changing the initial plasma temperature T_0 , which is taken to be $k_B T_0 = (0.08, 0.04, 0.02, 0.01)m_e c^2$, where k_B indicates the Boltzmann constant. The resulting β_0 values of our simulations are $\beta_0 \in \{0.32, 0.16, 0.08, 0.04\}$. We take the simulation with $\beta_0 = 0.08$ as the fiducial simulation.

3. RESULTS

In Fig. 1(a), we show a volume rendering of the current density (normalized to $J_{\text{rms}} = \langle J^2 \rangle^{1/2}$) from the fiducial simulation. Sheet-like current density structures are ubiquitous in the turbulent domain. Due to the presence of the mean field $\mathbf{B}_0 = B_0 \hat{\mathbf{z}}$, these structures are mostly elongated along $\hat{\mathbf{z}}$. As a result of magnetic reconnection, long and thin current sheets are characterized by the appearance of flux ropes, as shown in Fig. 1(b). As we show below, magnetic-field-aligned electric fields (E_{\parallel}) associated with magnetic reconnection play an important role in the early stages of electron energization. Finally, in Fig. 1(c), we show the one-dimensional spectra of the magnetic ($\delta \mathbf{B}$) and bulk velocity ($\delta \mathbf{V}$) fluctuations as a function of $k_{\perp} = (k_x^2 + k_y^2)^{1/2}$. Both power spectra approximately follow $P_{V,B}(k_{\perp}) \propto k_{\perp}^{-5/3}$ (Goldreich & Sridhar 1995) at $k_{\perp} d_i \lesssim 1$. At sub- d_i scales, $P_V(k_{\perp}) \propto k_{\perp}^{-2.8}$ down to $k_{\perp} d_e \sim 1$ (e.g. Alexandrova et al. 2009; Chen et al. 2014), and it further steepens for $k_{\perp} d_e \gtrsim 1$. A similar trend characterizes the $P_B(k_{\perp})$ spectrum, with the main difference that the steeper range occurs already at $k_{\perp} d_e \gtrsim 0.3$.

We show that a key outcome of the turbulent cascade is the generation of nonthermal particles for both ions and electrons. This is illustrated in Fig. 2, where we show the time evolution of the ion and electron energy spectra $f_s(\varepsilon) = dN(\varepsilon)/d\varepsilon$ (compensated by ε to emphasize the particle content) for the fiducial simulation. Here, $\varepsilon = (\gamma - 1)m_s c^2$ is the particle kinetic energy ($s = i, e$ for ions or electrons), with $\gamma = (1 - v^2/c^2)^{-1/2}$ indicating the particle Lorentz factor. As a result of turbulent field dissipation, the spectral peak shifts to higher energies. The shift is bounded by the magnetic energy available per each ion-electron pair, $\Delta \bar{\varepsilon}_{i,e} = \delta B_0^2/8\pi n_0 = (\delta B_0/B_0)^2 k_B T_{i0}/\beta_{i0} = 0.5 m_e c^2$. In addition, a significant number of particles increase in energy by $\Delta \varepsilon \gg \Delta \bar{\varepsilon}_{i,e}$. At late times, when most of the turbulent energy has decayed, the spectra of both ions and electrons extend well beyond the peak into a nonthermal tail of high-energy particles that can be described by a power law $f_s(\varepsilon)d\varepsilon \propto \varepsilon^{-p}d\varepsilon$ for $\varepsilon_{\min} < \varepsilon < \varepsilon_{\max}$, and a cutoff for $\varepsilon \geq \varepsilon_{\max}$.

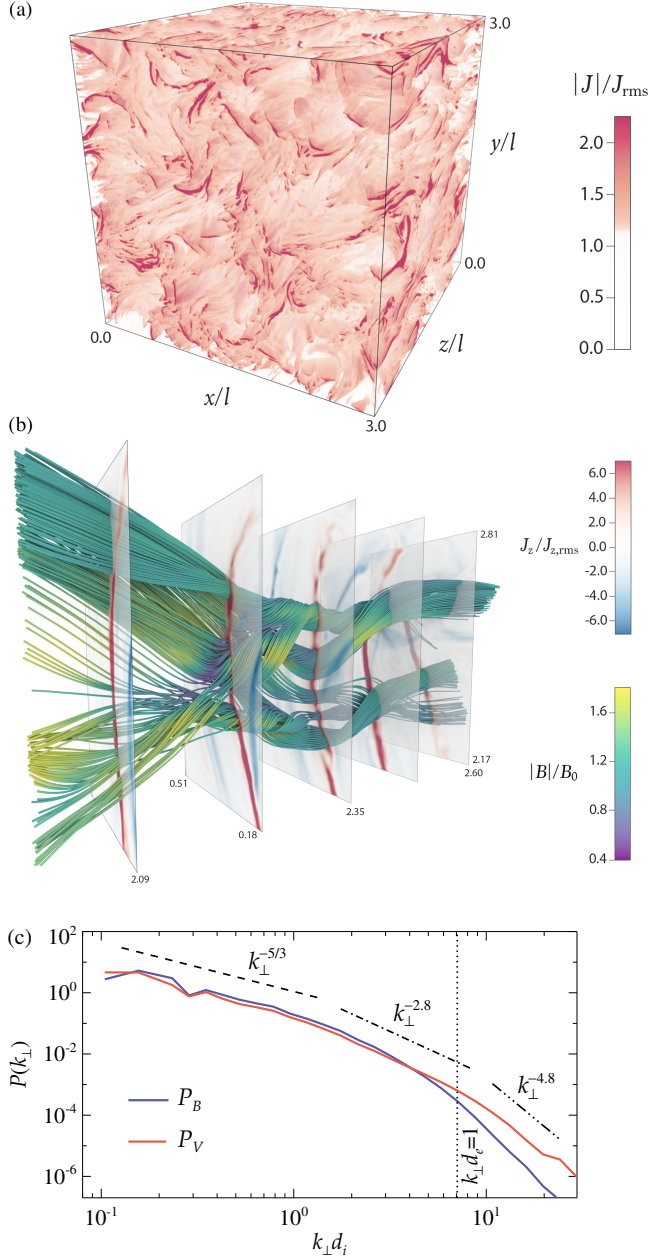


Figure 1. (a) Volume rendering of the current density $|J|$ at $t = 1.25 l/v_A$ from the fiducial simulation ($\beta_0 = 0.08$). (b) Zoomed-in subdomain with five $x-y$ slices at different z showing the current density J_z , along with selected magnetic field lines illustrating the presence of magnetic flux ropes. (c) One-dimensional k_{\perp} energy spectra of magnetic (blue) and velocity (red) fluctuations at $t = 1.25 l/v_A$. Different spectral slopes are provided for reference.

The slope p of the power law depends on β_0 . This is shown in the insets (top for ions, bottom for electrons) of Fig. 2. To facilitate the comparison of the different β_0 cases, we normalize ε by the mean energy per particle after turbulent dissipation, $\varepsilon_* = \varepsilon_{\text{th},0} + \kappa \Delta \bar{\varepsilon}_{i,e} =$

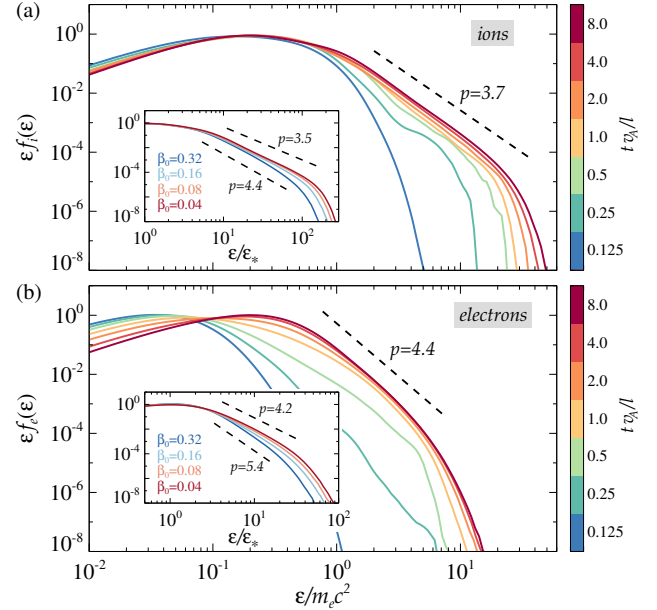


Figure 2. Evolution of the particle energy spectra for (a) ions ($s = i$) and (b) electrons ($s = e$) from the fiducial simulation ($\beta_0 = 0.08$). Power-law slopes $p = -d \log f_s / d \log \varepsilon$ for the nonthermal tail at late times are shown for reference. The insets show the late-time ion (top) and electron (bottom) energy spectra for simulations with $\beta_0 \in \{0.32, 0.16, 0.08, 0.04\}$.

$(3/2 + 2\kappa/\beta_0)k_B T_0$, where $\varepsilon_{\text{th},0} = (3/2)k_B T_0$ is the initial thermal energy and κ is the fraction of magnetic energy transferred to a given species (we take $\kappa = 1/3$ for both ions and electrons, since about 2/3 of the turbulent magnetic energy is equally distributed between ions and electrons by the end of the simulations). As observed in simulations of low- β magnetic reconnection (Dahlin et al. 2015; Li et al. 2019; Zhang et al. 2021), the spectrum hardens with decreasing β_0 , with the ion slope approaching $p \approx 3.5$ and the electron slope approaching $p \approx 4.2$ for $\beta_0 = 0.04$.¹

An important difference between energized ions and electrons is encoded by the distribution of the pitch angle α , i.e., the angle between the particle velocity and the local magnetic field. In Fig. 3(a), we show the probability density functions (PDFs) of the pitch-angle cosine $\cos \alpha = \mathbf{v} \cdot \mathbf{B} / (|\mathbf{v}| |\mathbf{B}|)$. While ions exhibit

¹ The power-law slope depends also on $\delta B_0/B_0$, and one might speculate that previous PIC and hybrid-PIC simulations of plasma turbulence (e.g. Grošelj et al. 2018; Arzamasskiy et al. 2019; Cerri et al. 2021) have not identified the development of nonthermal power-law tails due to the lower $\delta B_0/B_0$ values considered in those simulations, leading to steeper slopes (see Comisso & Sironi (2018, 2019); Comisso et al. (2020) for the effects of $\delta B_0/B_0$ on the particle energy distribution in magnetically dominated plasmas).

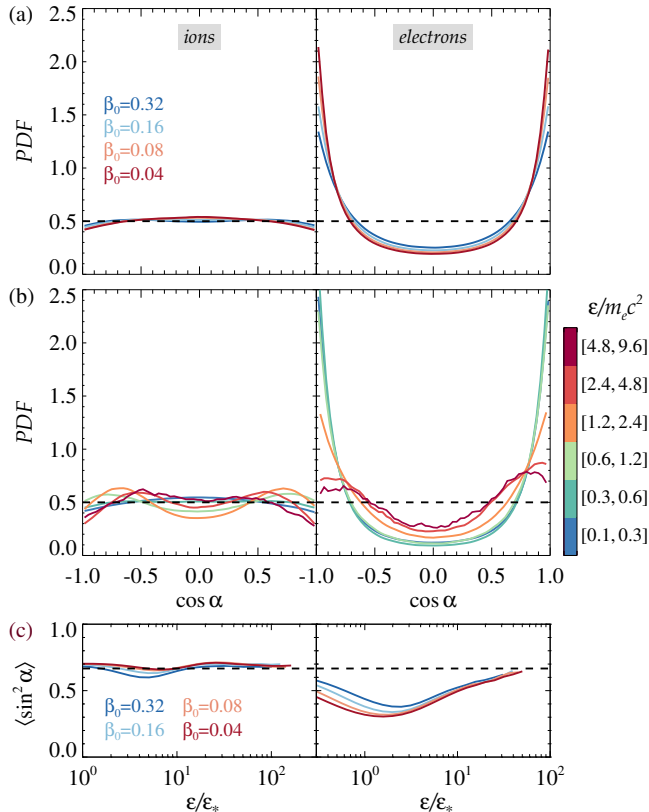


Figure 3. (a) PDFs of $\cos \alpha$ for simulations with $\beta_0 \in \{0.32, 0.16, 0.08, 0.04\}$. (b) PDFs of $\cos \alpha$ for particles with kinetic energy in different energy intervals for the simulation with $\beta_0 = 0.08$. (c) $\langle \sin^2 \alpha \rangle$ as a function of particle kinetic energy (normalized by ε_*) for simulations with different β_0 . All plots are obtained from data in the time range $tv_A/l \in [2, 6]$. Horizontal dashed black lines indicate the expectation for isotropic particles.

roughly isotropic PDFs, electrons are highly anisotropic with PDFs strongly peaked at $\cos \alpha = \pm 1$, i.e., electrons move mostly along the magnetic field lines. The different β_0 cases display a similar behavior, apart from the fact that electrons have higher PDF peaks near $\cos \alpha = \pm 1$ for lower β_0 . As we show below, this trend is due to the fact that electrons gain more energy from E_{\parallel} as β_0 decreases.

The PDFs shown in Fig. 3(a) are dominated by particles near the peak of $\varepsilon f_s(\varepsilon)$, since these particles control the number census. To characterize the anisotropy of higher-energy particles, we construct PDFs of $\cos \alpha$ for particles in different energy ranges. Fig. 3(b) shows those PDFs for the fiducial simulation. At moderate energies, $\varepsilon \lesssim \varepsilon_{\text{th},0} + \Delta \varepsilon_{i,e}$, ions and electrons display PDFs that are similar to those in Fig. 3(a). However, at higher energies the PDFs peak at intermediate values between $\cos \alpha = 0$ and $\cos \alpha = \pm 1$. This is particularly promi-

nent for electrons, which lose the \mathbf{B} -field alignment that characterizes low and moderate energies.

The significant energy dependence of the electron’s pitch-angle distribution is clearly displayed in Fig. 3(c), where we show $\langle \sin^2 \alpha \rangle$ as a function of ε (normalized by ε_*) for different β_0 values. Contrary to ions, the electron $\langle \sin^2 \alpha \rangle$ deviates significantly from the expected mean for an isotropic distribution, $\langle \sin^2 \alpha \rangle = 2/3$ (compare with the black dashed line) and attains a minimum at $\varepsilon/\varepsilon_* \sim 2$ (as in pair plasma turbulence (Comisso & Sironi 2019; Comisso et al. 2020; Comisso & Sironi 2021)). The value of $\langle \sin^2 \alpha \rangle$ increases for higher energies and eventually $\langle \sin^2 \alpha \rangle \sim 2/3$ for $\varepsilon \gg \varepsilon_*$ as a consequence of pitch-angle scatterings off the turbulent fluctuations.

To understand the difference between the energization of ions and electrons, and its effect on pitch angle anisotropy, we tracked the trajectories of a random sample of $\sim 10^8$ particles in each of the simulations. Figure 4(a) shows the time evolution of the kinetic energy for 5 representative ions and 5 representative electrons that eventually populate the high-energy end of the non-thermal tail in the fiducial simulation. These particles experience a sudden “injection phase,” i.e., an episode of rapid energy gain that brings them to energies much higher than the initial thermal energy (Comisso & Sironi 2018, 2019), followed by a more gradual energization phase akin to the stochastic Fermi acceleration mechanism (Fermi 1949).

We find that the injection stage occurs at sites where the current density at the particle location, J_p , is significantly above the average value. This is illustrated in Fig. 4(b), where we show the PDFs of $|J_p|/J_{\text{rms}}$ at the injection time t_{inj} (for ions and electrons that eventually end up with high energies), and at a generic time. Here, we identified t_{inj} as the time when low-energy particles ($\varepsilon < 0.5 m_e c^2$) have a rate of increase of the particle kinetic energy (averaged over $\Delta t = 150 \omega_{pe}^{-1}$) that satisfies the empirical threshold $\Delta \varepsilon / \Delta t \geq 0.2 R_{\text{rec}} v_A m_e c \omega_{pe}$, where $R_{\text{rec}} = 0.1$ is the normalized collisionless reconnection rate (Comisso & Bhattacharjee 2016; Cassak et al. 2017). For most particles, t_{inj} falls in the range $tv_A/l \sim 0.5 - 2$. One can see that the PDF of electrons at injection peaks at $|J_p|/J_{\text{rms}} \sim 2.5$, while the PDF of ions at injection peaks at a lower value of $|J_p|/J_{\text{rms}} \sim 1$. This should be contrasted with the PDF of the entire population of particles at a generic time, which peaks at $|J_p|/J_{\text{rms}} \sim 0$. Therefore, particle injection is associated with locations of high current density (current sheets).

The injection phase of ions and electrons is governed by different energization mechanisms (E_{\parallel} vs. E_{\perp}). In order to distinguish the role of the electric field par-

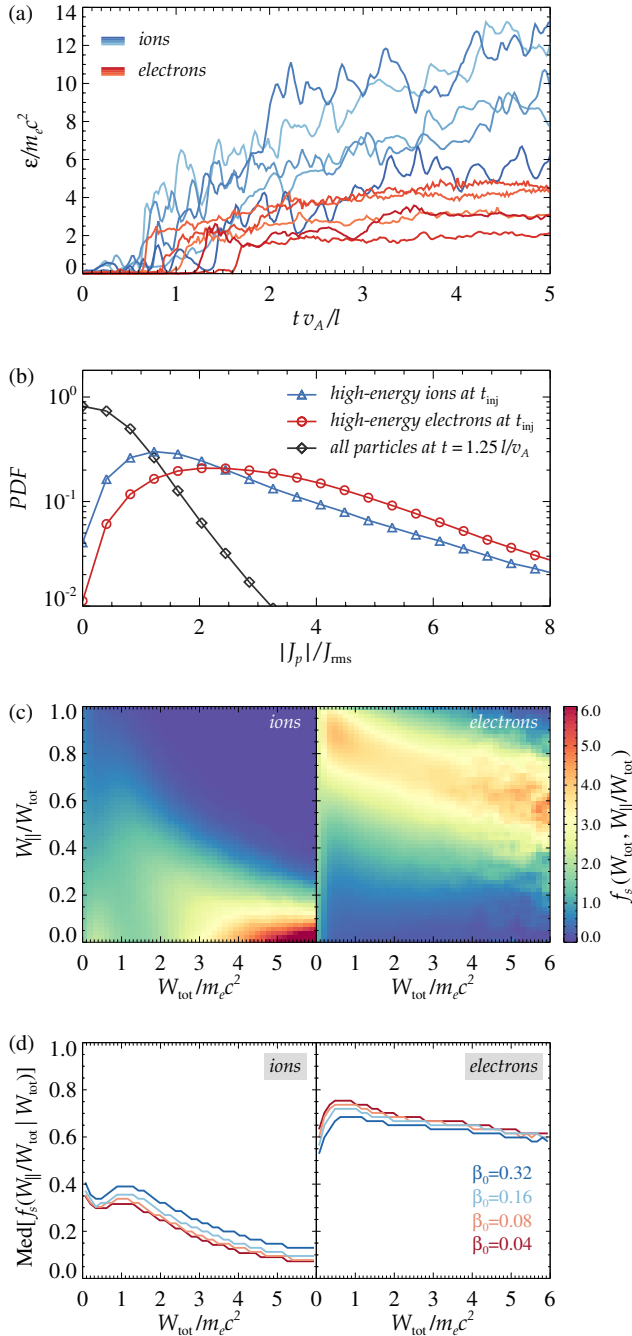


Figure 4. (a) Kinetic energy evolution for five representative ions (shades of blue) and five representative electrons (shades of red) that end up in the power-law range of the nonthermal tail. (b) PDFs of $|J_p|/J_{rms}$ experienced by high-energy ions (blue triangles) and high-energy electrons (red circles) at their t_{inj} and by all our tracked particles at $t = 1.25 l/v_A$ (black diamonds). (c) Distribution of ions (left) and electrons (right) with respect to W_{tot} and W_{\parallel}/W_{tot} , at the end of the $\beta_0 = 0.08$ simulation ($t = 8 l/v_A$). (d) Median of the conditional PDFs at given W_{tot} for ions (left) and electrons (right) at $t = 8 l/v_A$ from simulations with different β_0 .

allel (\parallel) and perpendicular (\perp) to the local magnetic field, we compute $W_{\parallel}(t) = q \int_0^t \mathbf{E}_{\parallel}(t') \cdot \mathbf{v}(t') dt'$ and $W_{\perp}(t) = q \int_0^t \mathbf{E}_{\perp}(t') \cdot \mathbf{v}(t') dt'$ for all the tracked particles. This allows us to construct the distributions $f_s(W_{tot}, W_{\parallel}/W_{tot})$, where $W_{tot} = W_{\parallel} + W_{\perp}$ is the work done by the total electric field. These distributions are shown in Fig. 4(c) for ions (left) and electrons (right) from the fiducial simulation. Ions gain energy almost entirely via E_{\perp} . In contrast, the injection of electrons is controlled by the E_{\parallel} field associated with reconnecting current sheets, while E_{\perp} energization from scatterings off the turbulent fluctuations becomes progressively more important as the electron energy increases.

The observed trend is robust across the different simulations. This is illustrated in Fig. 4(d), where we show the median of $f_s(W_{\parallel}/W_{tot} | W_{tot})$ for various β_0 values. The contribution of E_{\perp} consistently increases with energy in the range of the high-energy nonthermal tail, for both ions and electrons. However, low-energy electrons need to be first accelerated via E_{\parallel} up to the characteristic energy $\varepsilon/\varepsilon_* \sim 2$ (Fig. 3(c)) associated with magnetic reconnection. This is also the reason why the electron pitch-angle distribution develops a strong anisotropy, with $\min\langle \sin^2 \alpha \rangle$ attained at the same energy $\varepsilon/\varepsilon_* \sim 2$. For electrons, the initial energy gain via E_{\parallel} increases with decreasing β_0 , which is also consistent with the observed increase in pitch-angle anisotropy.

4. SUMMARY

In summary, we have demonstrated with 3D fully kinetic simulations that magnetized plasma turbulence is a viable mechanism for ion and electron acceleration. Both species develop nonthermal power-law tails, but ions attain harder nonthermal spectra and reach higher energies than electrons. For both species, the power-law slope becomes harder when decreasing the plasma β , i.e., the ratio of plasma pressure to magnetic pressure. We show that the energization of electrons is accompanied by a significant energy-dependent pitch-angle anisotropy, with most electrons moving parallel to the local magnetic field, while ions stay roughly isotropic. We demonstrate that particle injection from the thermal pool occurs in regions of high current density. Parallel electric fields associated with magnetic reconnection are responsible for the initial energy gain of electrons — which also imprints into their pitch-angle anisotropy — whereas perpendicular electric fields control the overall energization of ions. The results of our first-principles simulations shed light on the origin of nonthermal particles in space and astrophysical systems.

ACKNOWLEDGMENTS

We acknowledge fruitful discussions with Daniel Grošelj, Ramesh Narayan, Joonas Nättilä, and Emanuele Sobacchi. We are particularly grateful to Nina McCurdy/NASA Ames for helping with the visualizations. This research acknowledges support from NASA 80NSSC18K1285, NSF PHY-1903412, DOE DE-SC0021254, and the Cottrell Fellowship Award RCSA 26932. The simulations were performed on Columbia University (Ginsburg), NASA-HEC (Pleiades), and NERSC (Cori) resources.

REFERENCES

- Achterberg, A. 1981, *Astron. Astrophys.*, 97, 259
- Alexandrova, O., Saur, J., Lacombe, C., Mangeney, A., Mitchell, J., Schwartz, S.J., & Robert, P. 2009, *PhRvL*, 103, 763 165003
- Arzamasskiy, L., Kunz, M. W., Chandran, B. D. G., & Quataert, E. 2019, *ApJ*, 879, 53
- Arzner, K., & Vlahos, L. 2004, *ApJL*, 605, L69
- Arzner, K., Knaepen, B., Carati, D., Denewet, N., & Vlahos, L. 2006, *ApJ*, 637, 322
- Beresnyak, A., & Li, H. 2016, *ApJ*, 819, 90
- Bieber, J. W., & Matthaeus, W. H. 1997, *ApJ*, 485, 655
- Birdsall, C. K., & Langdon, B. 1985, *Plasma Physics via Computer Simulation* (McGraw-Hill)
- Blandford, R., Meier, D., & Readhead, A. 2019, *Ann. Rev. Astron. Astrophys.*, 57, 467
- Brunetti, G., & Jones, T. W. 2014, *Int. J. Mod. Phys. D*, 23,1430007
- Buneman, O. 1993, in “Computer Space Plasma Physics: Simulation Techniques and Software”, Terra Scientific, Tokyo, 67
- Cassak, P. A., Liu, Y.-H., & Shay, J. 2017, *JPIPh*, 83, 715830501
- Cerri, S. S., Arzamasskiy, L., & Kunz, M. W. 2021, *ApJ*, 916, 120
- Chen, C. H. K., Leung, L., Boldyrev, S., Maruca, B. A., & Bale, S. D. 2014, *Geophys. Res. Lett.*, 41, 763 8081
- Comisso, L., & Bhattacharjee, A. 2016, *JPIPh*, 82, 595820601
- Comisso, L., & Sironi, L. 2018, *PhRvL*, 121, 255101
- Comisso, L., & Sironi, L. 2019, *ApJ*, 886, 122
- Comisso, L., Sobacchi, E., & Sironi, L. 2020, *ApJL*, 895, L40
- Comisso, L., & Sironi, L. 2021, *PhRvL*, 127, 255102
- Dahlin, J. T., Drake, J. F., & Swisdak, M. 2015, *PhPI*, 22, 100704
- Dalena, S., Rappazzo, A. F., Dmitruk, P., Greco, A., & Matthaeus, W. H. 2014, *ApJ*, 783, 143
- Dmitruk, P., Matthaeus, W. H., & Seenu, N. 2004, *ApJ*, 617, 667
- Fermi, E. 1949, *PhRv*, 75, 1169
- Goldreich, P., & Sridhar, S. 1995, *ApJ*, 438, 763
- González, C. A., Dmitruk, P., Mininni, P. D., & Matthaeus, W. H. 2017, *ApJ*, 850, 19
- Grošelj, D., Mallet, A., Loureiro, N.F., & Jenko, F. 2018, *PhRvL*, 120, 105101
- Hall, D. E., & Sturrock, P. A. 1967, *PhFl*, 10, 2620
- Jaekel, U., & Schlickeiser, R. 1992, *J. Phys. G*, 18, 1089
- Kennel, C. F., & Engelmann, F. 1966, *PhFl*, 9, 2377
- Kimura, S. S., Tomida, K., & Murase, K. 2019, *MNRAS*, 485, 163
- Kowal, G., de Gouveia Dal Pino, E. M., & Lazarian, A. 2012, *PhRvL*, 108, 241102
- Kulsrud, R. M., & Ferrari, A. 1971, *Ap&SS*, 12, 302
- Kunz, M. W., Stone, J. M., & Quataert, E. 2016, *PhRvL*, 117, 235101
- Islaker, H., Vlahos, L., & Constantinescu, D. 2017, *PhRvL*, 119, 045101
- Lazarian, A., Vlahos, L., Kowal, G., et al. 2012, *SSRv*, 173, 557
- Lehe, R., Parrish, I. J., & Quataert, E. 2009, *ApJ*, 707, 404
- Li, X., Guo, F., Li, H., Stanier, A., & Kilian, P. 2019, *ApJ*, 884, 118
- Lynn, J. W., Quataert, E., Chandran, B. D. G., & Parrish, I. J. 2014, *ApJ*, 791, 71
- Matthaeus, W. H., Qin, G., Bieber, J. W., & Zank, G. P. 2003, *ApJ*, 590, L53
- McComas, D.J., Christian, E.R., Cohen, C.M.S., et al. 2019, *Nature*, 576, 223

- Melrose, D. B. 1980, Plasma astrophysics. Nonthermal processes in diffuse magnetized plasmas - Vol. 1, 2 (New York: Gordon and Breach)
- Michalek, G., & Ostrowsky, M. 1996, Nonlinear Processes in Geophysics, 3, 66
- Nättilä, J., & Beloborodov, A. M. 2021, ApJ, 921, 87
- O'Sullivan, S., Reville, B., & Taylor, A. M. 2009, MNRAS, 400, 248
- Pecora, F., Servidio, S., Greco, A., et al. 2018, JPIPh, 84, 725840601
- Petrosian, V. 2012, SSRv, 173, 535
- Pezzi, O., Blasi, P., & Matthaeus, W. H. 2022, ApJ, 928, 25
- Reynolds, S. P. 2008, Ann. Rev. Astron. Astrophys., 46, 89
- Shalchi, A. 2006, Astron. Astrophys., 453, L43
- Sobacchi, E., Nättilä, J., & Sironi, L. 2021, MNRAS, 503, 688
- Spitkovsky, A. 2005, in AIP Conf. Ser., Vol. 801, Astrophysical Sources of High Energy Particles and Radiation, ed. T. Bulik, B. Rudak, & G. Madejski, 345
- Sun, X., & Bai, X.-N. 2021, MNRAS, 506, 1128
- Teraki, Y., & Asano, K. 2019, ApJ, 877, 71
- Trotta, D., Franci, L., Burgess, D., & Hellinger, P. 2020, ApJ, 894, 136
- Völk, H. J. 1973, Astrophys. Space Sci., 25, 471
- Wong, K., Zhdankin, V., Uzdensky, D. A., Werner, G. R., & Begelman, M. C. 2020, ApJL 893, L7
- Yan, H., & Lazarian, A. 2008, ApJ, 673, 942
- Yuan, F., & Narayan, R. 2014, ARA&A, 52, 529
- Zhang, Q., Guo, F., Daughton, W., Li, H., & Li, X. 2021, PhRvL, 127, 185101
- Zhdankin, V., Werner, G. R., Uzdensky, D. A., & Begelman, M. C. 2017, PhRvL, 118, 055103
- Zhdankin, V., Uzdensky, D. A., Werner, G. R., & Begelman, M. C. 2018, ApJ, 867, L18
- Zhdankin, V., Uzdensky, D. A., Werner, G. R., & Begelman, M. C. 2019, PhRvL, 122, 055101